SFN358 #43–56

#48 Time-variable Jet Ejections from RW Aur A, RY Tau, and DG Tau

#52 The interplay between forming planets and photo-evaporating discs I: Forbidden line diagnostics

48. **Time-Variable Jet Ejections from RW Aur A, RY Tau and DG Tau**

Michihiro Takami, Hans Moritz Guenther, P. Christian Schneider, Tracy L. Beck, Jennifer L. Karr, Youichi Ohyama, Roberto Galvan-Madrid, Taichi Uyama, Marc White, Konstantin Grankin, Deirdre Coffey, Chun-Fan Liu, Misato Fukagawa, Nadine Manset, Wen-Ping Chen, Tae-Soo Pyo, Hsien Shang, Thomas P. Ray, Masaaki Otsuka, Mei-Yin Chou

★ We present Gemini-NIFS, VLT-SINFONI and Keck-OSIRIS observations of near-infrared [Fe II] emission associated with the well-studied jets from three active T Tauri stars; RW Aur A, RY Tau and DG Tau taken from 2012-2021. We primarily covered the redshifted jet from RW Aur A, and the blueshifted jets from RY Tau and DG Tau, to investigate long-term time variabilities potentially related to the activities of mass accretion and/or the stellar magnetic fields. All of these jets consist of several moving knots with tangential velocities of 70-240 km s-1, ejected from the star with different velocities and at irregular time intervals. Via comparison with literature, we identify significant differences in tangential velocities for the DG Tau jet between 1985-2008 and 2008-2021. The sizes of the individual knots appear to increase with time, and in turn, their peak brightnesses in the 1.644-micron emission decreased up to a factor of 30 during the epochs of our observations. A variety of the decay timescales measured in the [Fe II] 1.644 micron emission can be attributed to different pre-shock conditions if the moving knots are unresolved shocks. However, our data do not exclude the possibility that these knots are due to non-uniform density/temperature distributions with another heating mechanism, or in some cases due to stationary shocks without proper motions. Spatially resolved observations of these knots with significantly higher angular resolutions are necessary to better understand their physical nature.

- 質量降着や星間磁場の活動に関連していると考えられている、YSOジェットの長期変動を調べる
- 2012年から2021年にかけて行われた3つのT Tauri星 (RW Aur A、RY Tau、DG Tau) からのジェットの近赤外線[Fe II]輝線観測 (Gemini-NIFS・SINFONI・Keck-OSIRIS)

観測

- ターゲット
  - RW Aur A … 双極ジェットのうち明るい赤方偏移ジェット
  - RY TauとDG Tau … 観測可能な青方偏移ジェット

- 近赤外線[Fe II]放射の分光観測（R = 3000-5500, Δv = 55-100 km/s）

Table 1
Targets

Star	Distance[a] (pc)	Stellar Mass ($M_\odot$)	Age (Myr)	Mass Accretion Rate ($10^{-7}\ M_\odot\ yr^{-1}$)	v_{sys}[b] (km s^{-1})	References[c]
RW Aur A	156 ± 1[d]	1.4 ± 0.2	4 ± 2	0.3	20	1
RY Tau	125 ± 2	2.0 ± 0.3	6 ± 2	0.2–1.4	18	2, 3
DG Tau	138 ± 4	~1	~1	0.5–8	16	1, 4, 5, 6

Table 2
Instruments

Telescope and Instrument	Operation	IFU and (Selected) Sampling	Grating	Spectral Coverage (μm)	Spectral Resolution R	Field of View (FOV)
Gemini-NIFS	Queue	Slit Slicer, $0\farcs1 \times 0\farcs04$	H	1.49–1.80	5300	$3\farcs0 \times 3\farcs0$
VLT-SINFONI	Queue	Slit Slicer, $0\farcs1 \times 0\farcs05$	H	1.45–1.85	3000	$3\farcs6 \times 3\farcs3$
Keck-OSIRIS	Classical	Lenslet, $0\farcs05$	Hn3	1.59–1.67	3800	$3\farcs2 \times 2\farcs4$

Table 3
Log of the Observations

Star	Date	Instrument	Run ID (PI)	Photometrically Accurate[a]	t_{exp} (s)	n_{exp}	Core FWHM (arcseconds)	f_{core}[b]	Range of Integration[c]	
									v (km s^{-1})	Y[d] (arcseconds)
RW Aur A	2012 Oct 20	NIFS[e]	GN-2012B-Q-99 (Beck)	°	600	9	0.16	0.61	30 to 180	−0.15 to +0.15
	2014 Feb 28	NIFS	GN-2014A-Q-29 (Günther)	°	60	12	0.15	0.48	30 to 180	−0.15 to +0.15
	2014 Dec 29	NIFS	GN-2014B-Q-18 (Günther)	°	84	20	0.15	0.45	30 to 180	−0.15 to +0.15
	2017 Feb 15	NIFS	GN-2017A-FT-1 (Takami)	°	55	36	0.15	0.49	30 to 180	−0.15 to +0.15
	2017 Dec 8	SINFONI	2100.C-5015(A) (Takami)		4	140	0.10	0.24	−20 to 230	−0.15 to +0.15
	2017 Dec 11	SINFONI	2100.C-5015(A) (Takami)		4	140	0.10	0.26	−20 to 230	−0.15 to +0.15
	2018 Aug 21	NIFS	GN-2018B-Q-141 (Takami)		55	17	0.14	0.46	30 to 180	−0.15 to +0.15
	2018 Aug 31	NIFS	GN-2018B-Q-141 (Takami)	°	55	3	0.12	0.51	30 to 180	−0.15 to +0.15
	2018 Sep 16	NIFS	GN-2018B-Q-141 (Takami)		55	19	0.12	0.50	30 to 180	−0.15 to +0.15
	2019 Oct 7	NIFS	GN-2019B-Q-132 (Takami)		55	36	0.16	0.46	30 to 180	−0.15 to +0.15
	2021 Feb 3	OSIRIS	S21A0039N/S364 (Takami)	°	24	30	0.05–0.10[f]	~0.3[f]	10 to 190	−0.15 to +0.15
RY Tau	2012 Oct 27	NIFS[e]	GN-2012B-Q-99 (Beck)	°	600	10	0.14	0.52	−170 to −40	−0.25 to +0.25
	2014 Feb 28	NIFS	GN-2014A-Q-29 (Günther)	°	15	30	0.18	0.35	−170 to −40	−0.25 to +0.25
	2014 Dec 29	NIFS	GN-2014B-Q-18 (Günther)	°	15	54	0.18	0.46	−170 to −40	−0.25 to +0.25
	2017 Feb 18	NIFS	GN-2017A-FT-1 (Takami)	°	15	105	0.12	0.46	−170 to −40	−0.25 to +0.25
	2018 Aug 17	NIFS	GN-2018B-Q-141 (Takami)	°	15	99	0.15	0.37	−170 to −40	−0.25 to +0.25
	2019 Oct 23	NIFS	GN-2019B-Q-132 (Takami)		15	108	0.13	0.53	−170 to −40	−0.25 to +0.25[g]
	2021 Feb 3	OSIRIS	S21A0039N/S364 (Takami)		19	46	0.05–0.10[f]	~0.4[f]	−160 to −30	−0.2 to +0.2[g]
DG Tau	2013 Feb 9	NIFS[e]	GN-2012B-Q-32 (McGregor)	°	600	6	0.16	0.61	−240 to −70	−0.3 to +0.3
	2014 Feb 28	NIFS	GN-2014A-Q-29 (Günther)	°	45	12	0.12	0.50	−240 to −70	−0.3 to +0.3
	2014 Dec 29	NIFS	GN-2014B-Q-18 (Günther)	°	45	27	0.14	0.37	−240 to −70	−0.3 to +0.3
	2017 Feb 17	NIFS	GN-2017A-FT-1 (Takami)	°	25	72	0.11	0.44	−240 to −70	−0.3 to +0.3
	2017 Dec 22	SINFONI	2100.C-5015(A) (Takami)		4	140	0.11	0.18	−240 to −40	−0.3 to +0.3
	2017 Dec 25	SINFONI	2100.C-5015(A) (Takami)		4	140	0.11	0.20	−240 to −40	−0.3 to +0.3
	2018 Nov 27	NIFS	GN-2018B-Q-141 (Takami)	°	25	72	0.12	0.48	−240 to −70	−0.3 to +0.3
	2019 Oct 17	NIFS	GN-2019B-Q-132 (Takami)	°	25	84	0.16	0.37	−240 to −70	−0.3 to +0.3

結果

- ジェットノットの識別のため、観測エポックに応じてジェット軸方向に移動させた。
- ノット放出は不規則な時間間隔を示す。

Offset = 0.2/yr　RW Aur A　ノット速度= 120-220[km/s]
放出間隔 = 300-2000[day]

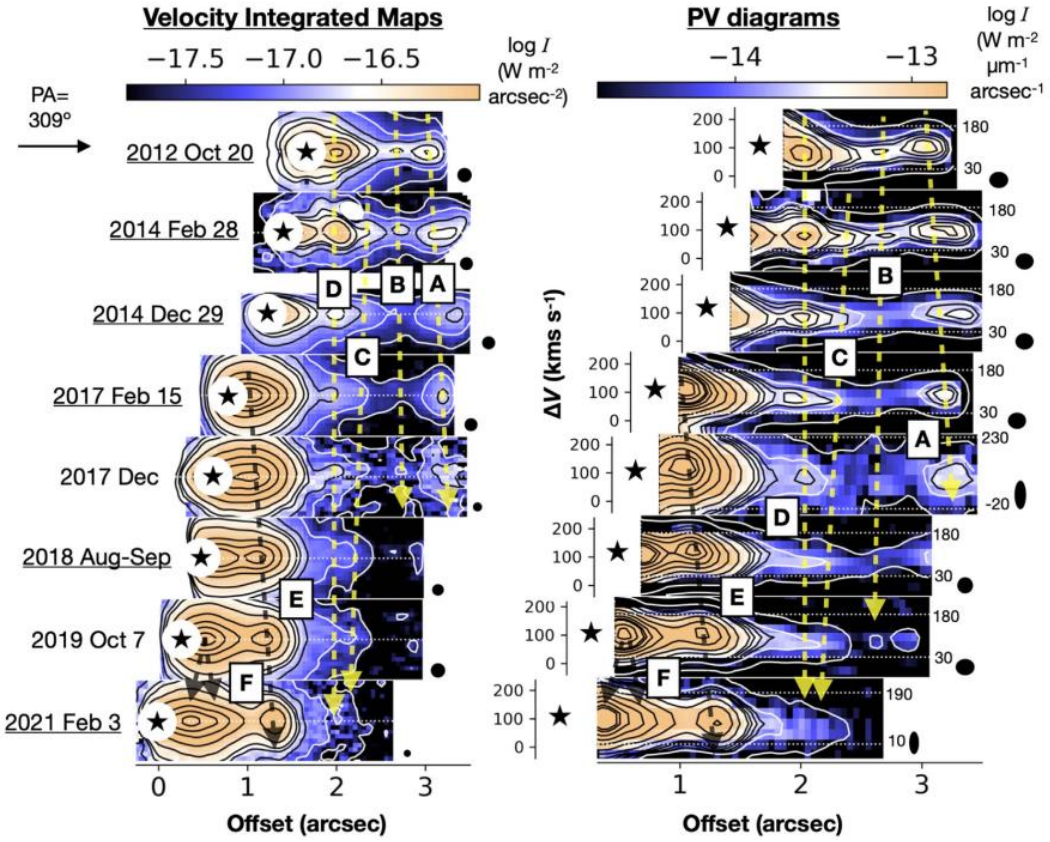

Offset = 0.3/yr　RY Tau　ノット速度 = 120-240[km/s]
放出間隔 = 300-1200[day]

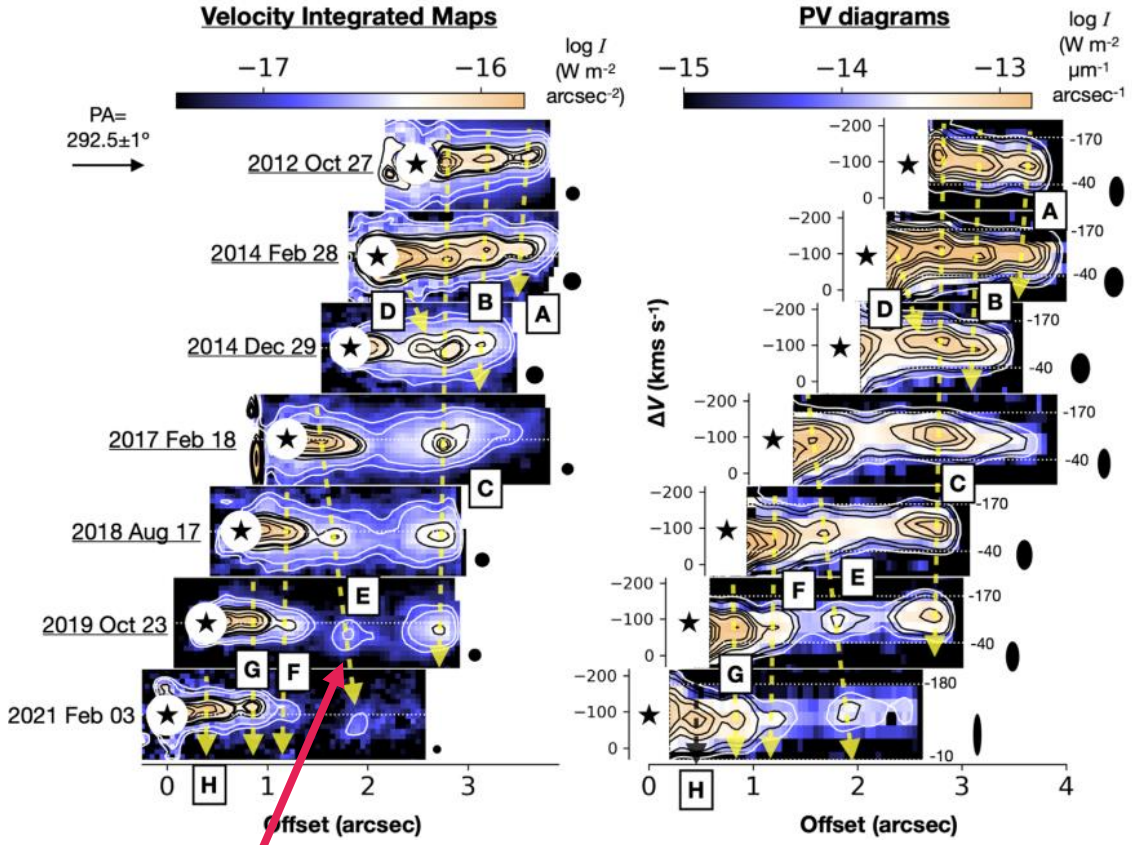

Knot Eは特に軸からのずれが大きい (0.1°); wiggling motions of the jet

ノットの時間変化

空間オフセット

Knot C-Eは
今後衝突？

Knot C,Dは
過去に衝突

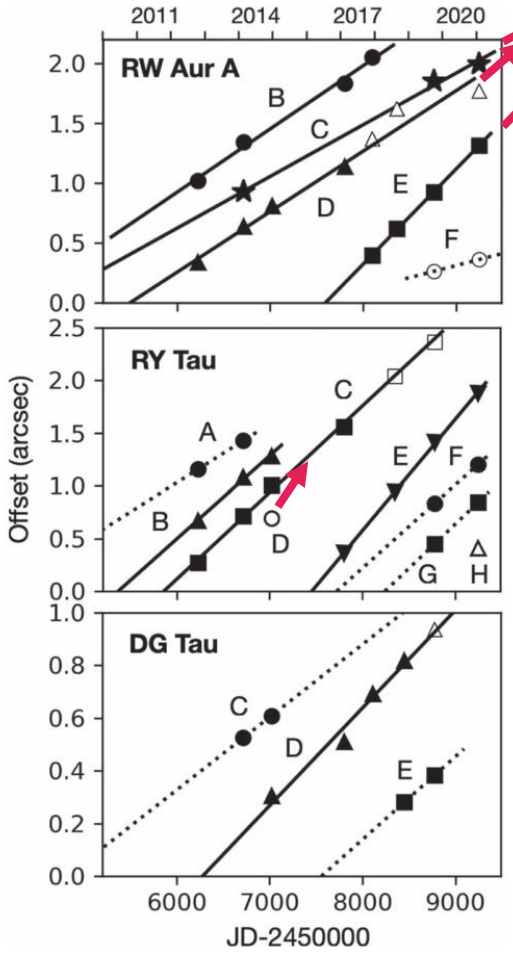

Figure 4. The proper motions measured for the individual knots. The dots with filled symbols are used for fitting. The solid lines show reliable fittings, while the dotted lines are tentative, due to limited epochs of observations. The error bar for each dot is not shown, as there is no straightforward definition relating to the given method of the measurements (see the text).

ノットの1.644μmピーク強度 (オフセット距離 = 時間変化)

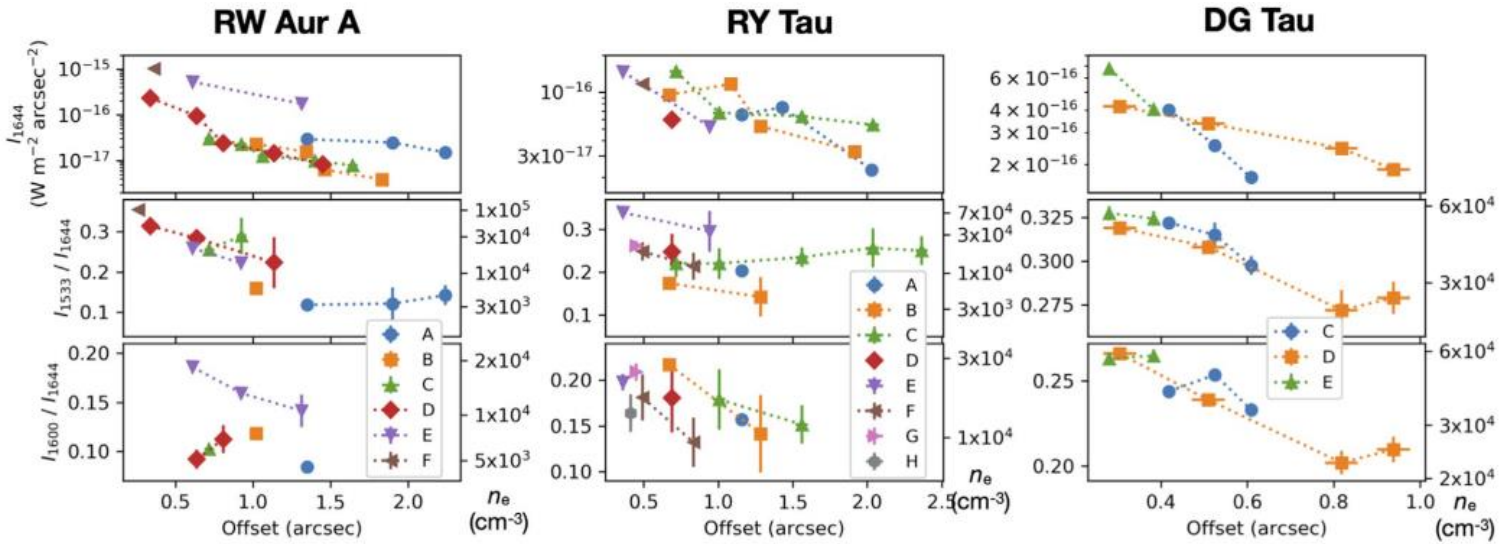

Figure 6. The [Fe II] 1.644 μm peak intensities (top), the $I_{1.533\mu m}/I_{1.644\mu m}$ intensity ratios (middle), and the $I_{1.600\mu m}/I_{1.644\mu m}$ intensity ratios as a function of the distance to the star. See the text for the selection criteria for the plotted data. For the intensity ratios, we show the corresponding electron densities for $T_e = 10^4$ K to the right of the individual panels. Some dots are associated with the horizontal error bars, based on the uncertainties tabulated in Tables 4–6. The vertical error bars are only shown when they are larger than the dots. See the text for other details.

- ピーク強度は観測期間内で最大30倍減少
- 強度減衰のタイムスケール

$$I_1 = I_0 \exp(-t/t_{\rm decay}),$$

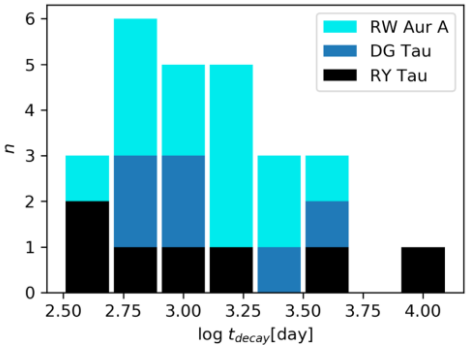

ジェット速度の長期変動

- 本研究と過去の研究で調べられたジェットの固有運動を比較すると、
  - RW Aur A・RY Tauからのジェットはほぼ同じ
  - DG Tauからのジェットは過去の値より2倍ほど小さい

Table 7
Proper Motions of Jet Knots

Star	Proper Motion (arcsec yr^{-1})	V_{tan} (km s^{-1})	Angular Distance from the Star	Lines[a]	Approximate Years of Ejections From the Star	References[b]
RW Aur A	0.15–0.23	110–170	0.″3–20″	[Fe II], [S II], Hα	1830–2000	1
	0.16–0.24	120–180	1″–3″	[S II]	1930–2000	2
	0.16–0.29	120–210	0.″2–3″	[Fe II]	2007–2020	This work
RY Tau	0.3–0.4	180–240	1″–6″	[Fe II]	1980–2010	3
	0.2–0.4	120–240	0.″2–2.″5	[Fe II]	2007–2020	This work
	~0.3	~200	0.″15–1″	[Fe II], Hα	2019–2021	4
DG Tau	0.3	200	~0.″3	[O I]	1985	5
	0.27–0.3	180–200	0.″1–3.″5	various	1995–2000	6
	0.17–0.33	110–220	0.″2–1.″4	[Fe II]	1998–2004	7
	0.10–0.14	70–90	0.″2–2″	[Fe II]	2008–2020	This work

Notes.
[a] [Fe II] 1.644 μm, [S II] 6731 Å, and [O I] 6300 Å for the forbidden lines.
[b] (1) Berdnikov et al. (2017); (2) Lopez-Martin et al. (2003); (3) Garufi et al. (2019); (4) Uyama et al. (2022); (5) Dougados et al. (2000); (6) Pyo et al. (2003); and (7) White et al. (2014b).

52. **The interplay between forming planets and photo-evaporating discs I: Forbidden line diagnostics**

Michael L. Weber, Barbara Ercolano, Giovanni Picogna, Christian Rab ★

Disc winds and planet formation are considered to be two of the most important mechanisms that drive the evolution and dispersal of protoplanetary discs and in turn define the environment in which planets form and evolve. While both have been studied extensively in the past, we combine them into one model by performing three-dimensional radiation-hydrodynamic simulations of giant planet hosting discs that are undergoing X-ray photo-evaporation, with the goal to analyse the interactions between both mechanisms. In order to study the effect on observational diagnostics, we produce synthetic observations of commonly used wind-tracing forbidden emission lines with detailed radiative transfer and photo-ionisation calculations. We find that a sufficiently massive giant planet carves a gap in the gas disc that is deep enough to affect the structure and kinematics of the pressure-driven photo-evaporative wind significantly. This effect can be strong enough to be visible in the synthetic high-resolution observations of some of our wind diagnostic lines, such as the [OI] 6300 A or [SII] 6730 A lines. When the disc is observed at inclinations around 40 deg and higher, the spectral line profiles may exhibit a peak in the redshifted part of the spectrum, which cannot easily be explained by simple wind models alone. Moreover, massive planets can induce asymmetric substructures within the disc and the photo-evaporative wind, giving rise to temporal variations of the line profiles that can be strong enough to be observable on timescales of less than a quarter of the planet's orbital period.

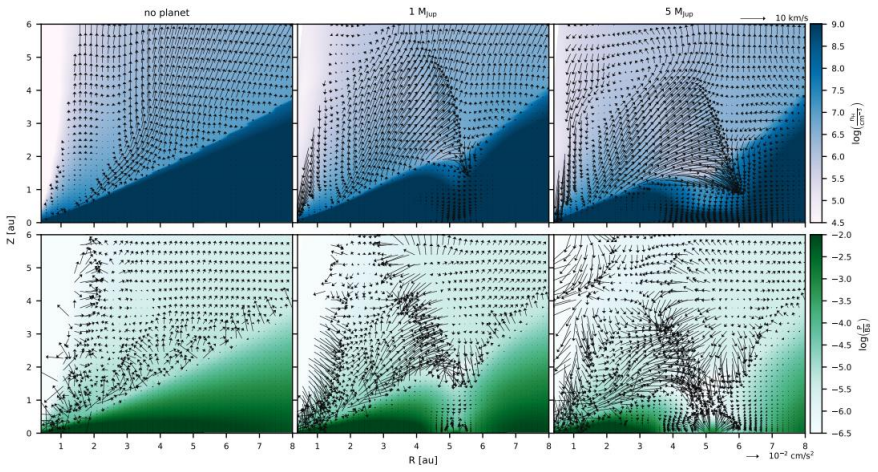

Figure 2. Top panels: Azimuthally averaged hydrogen number density (background color) and velocity field (black arrows). Bottom panels: Azimuthally averaged gas pressure (background color) and the effective acceleration as the sum of the gravitational acceleration towards the central star, the acceleration caused by the pressure-gradient force and the centrifugal acceleration. The velocity and acceleration fields are only plotted where the number density exceeds $2 \cdot 10^5$ cm^{-3}.

- 「円盤風」と「惑星形成」は原子惑星系円盤の進化・拡散を駆動する重要メカニズム
- 両者の相互作用を調べるため、X線光蒸発を受けている巨大惑星を含む円盤の3次元輻射流体シミュレーションを行った
- 十分に質量のある巨大惑星は、圧力駆動の光蒸発風の構造・運動に影響を与えるほど深い円盤ギャップを作ることがわかった

3D model of a disc with X-ray photo-evaporation and a giant planet

1. 惑星なし円盤の構造を計算 (Model REF)
2. 惑星 (M_p = 1, 5 [M_J]) をR_p = 5.2 [au] (太陽系木星軌道) に置き、円盤構造がほぼ定常状態になるまで時間を進める (Model MJ1, MJ5)
3. 合成禁制輝線として、一般的に観測される [OI] 6300 Å, [SII] 4068 Å, [SII] 6730 Å and [NeII] 12.8 μm, [FeII] 17.2 μmを選択・計算した。

Parameter	Value	Model-ID
M_{planet}	0	REF
	1 M_J	MJ1
	5 M_J	MJ5
M_*	0.7 $M_\odot$	
M_{disc}	$\approx 0.1\ M_*$	
α (viscosity parameter)	10^{-3}	
γ (adiabatic index)	1.4	
μ (mean molecular weight)	1.37125	
L_X [erg/s]	$2 \cdot 10^{30}$ erg/s	

Table 1. Model parameters for the hydrodynamical models. We name the 2D reference model with no planet REF, the other two models that include a planet are named MJ1 and MJ5, according to the planet's mass.

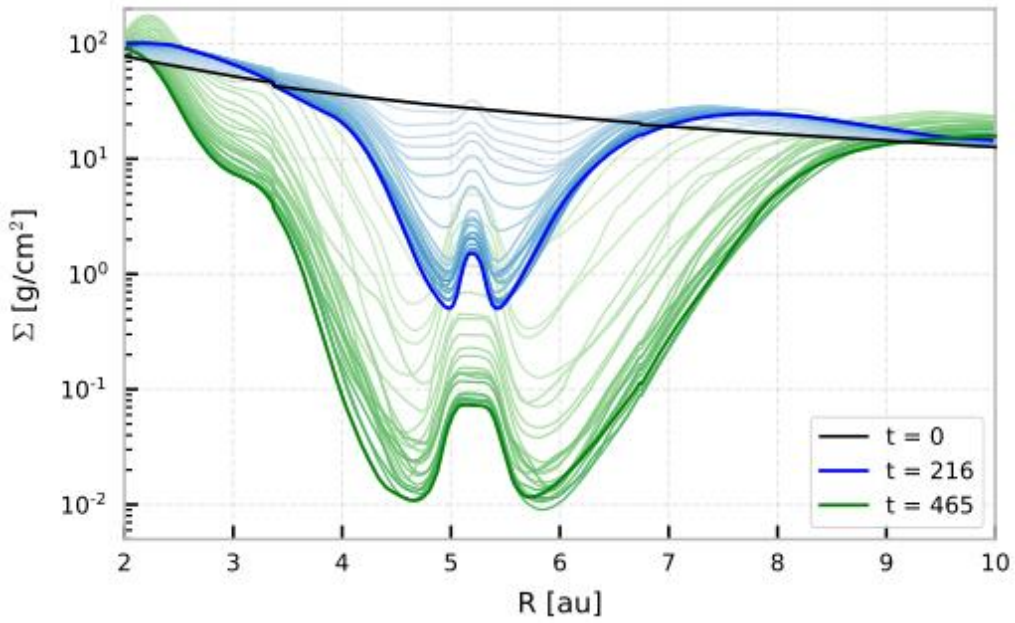

Figure 1. Surface density in steps of 10 orbits starting at the time of planet insertion (t = 0), which is represented by the lightest blue line. The dark blue line at t = 216 orbits represents the surface density of the MJ1 model. At the same time, it serves as the starting point for the MJ5 model (green lines), which was evolved for another 249 orbits until t = 465.

円盤風の構造と運動

惑星は円盤風を駆動する圧力勾配を変化させる。
惑星上空では密度が低下した領域ができ、この領域から物質が落下する。
(圧力勾配によらない円盤風(例えば磁気風)に同様の効果があるかはまだ不明。)

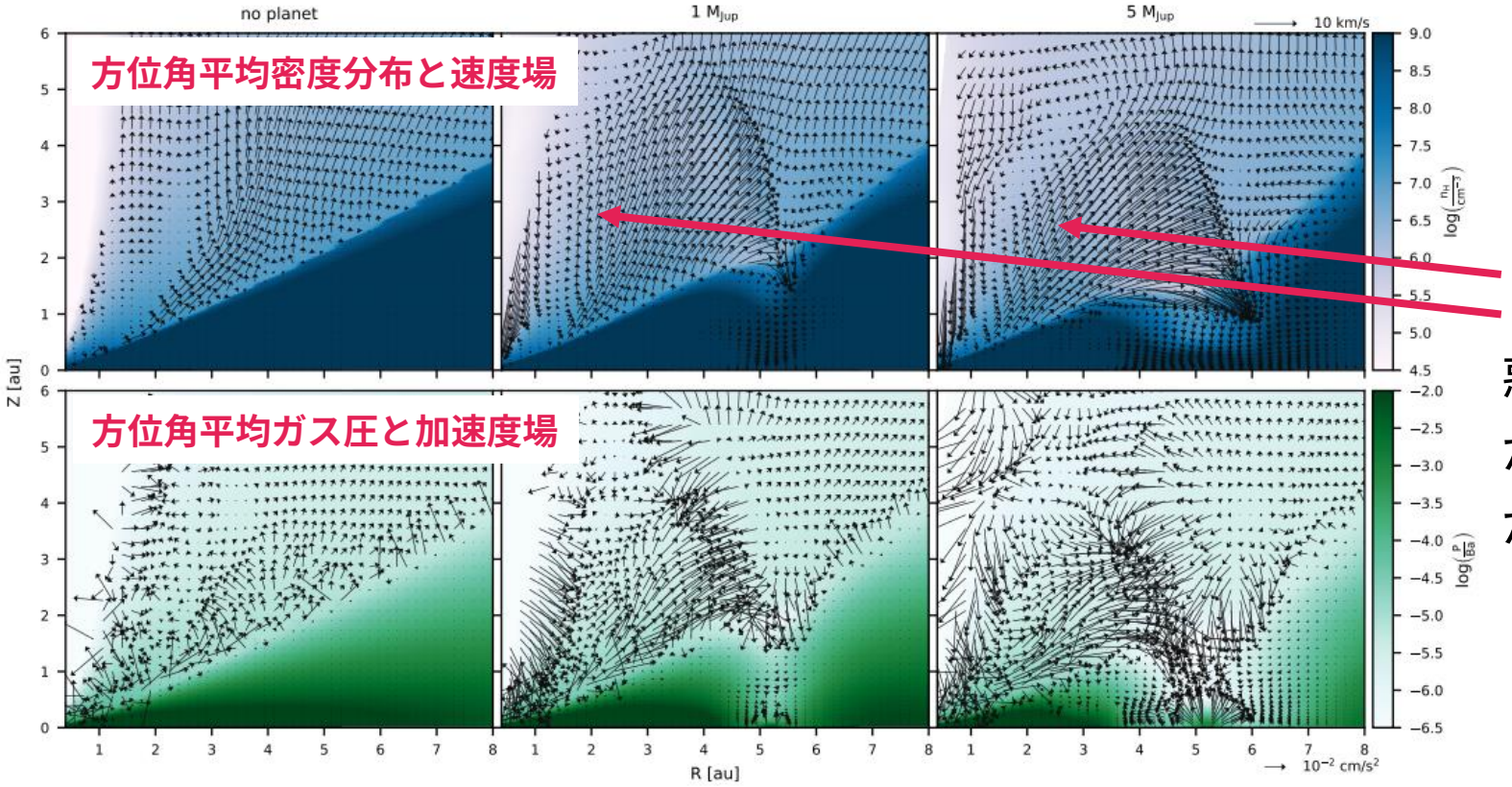

Figure 2. Top panels: Azimuthally averaged hydrogen number density (background color) and velocity field (black arrows). Bottom panels: Azimuthally averaged gas pressure (background color) and the effective acceleration as the sum of the gravitational acceleration towards the central star, the acceleration caused by the pressure-gradient force and the centrifugal acceleration. The velocity and acceleration fields are only plotted where the number density exceeds $2 \cdot 10^5$ cm^{-3}.

惑星を持つモデル(密度が低下)の方が圧力勾配が大きくなり、円盤風が内側から急角度で噴き出す。

輝線放射領域

輝線毎に円盤風の異なる領域を分析したい

85%の放射が発生しているコントアを表示

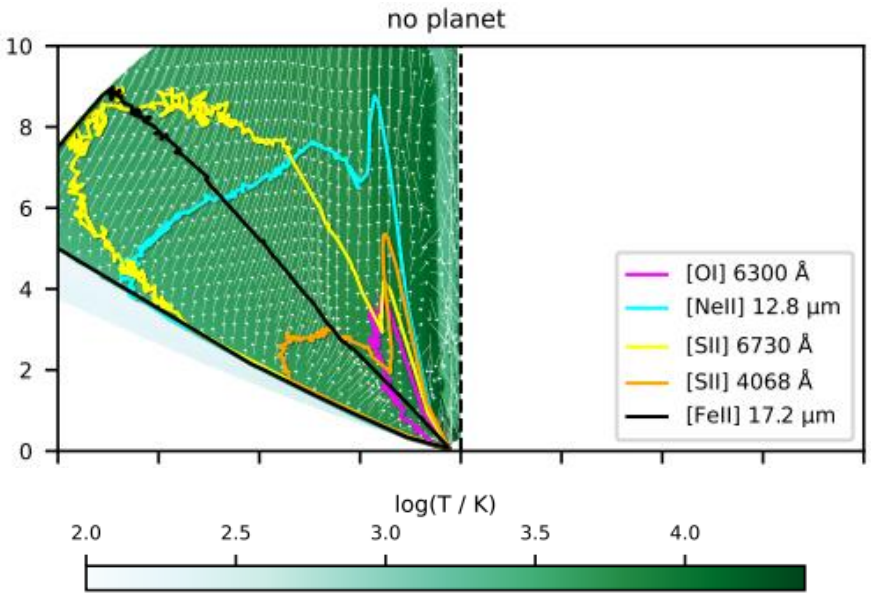

Figure 4. 85% emission regions of our chosen diagnostic lines. The left halves show the azimuthal average, the right halves show a cut through the y=0 plane, where the planet is located. The background colour indicates the temperature that was calculated with MOCASSIN. The white arrows indicate the velocity field of the wind.

方位角平均　　惑星を含む断面

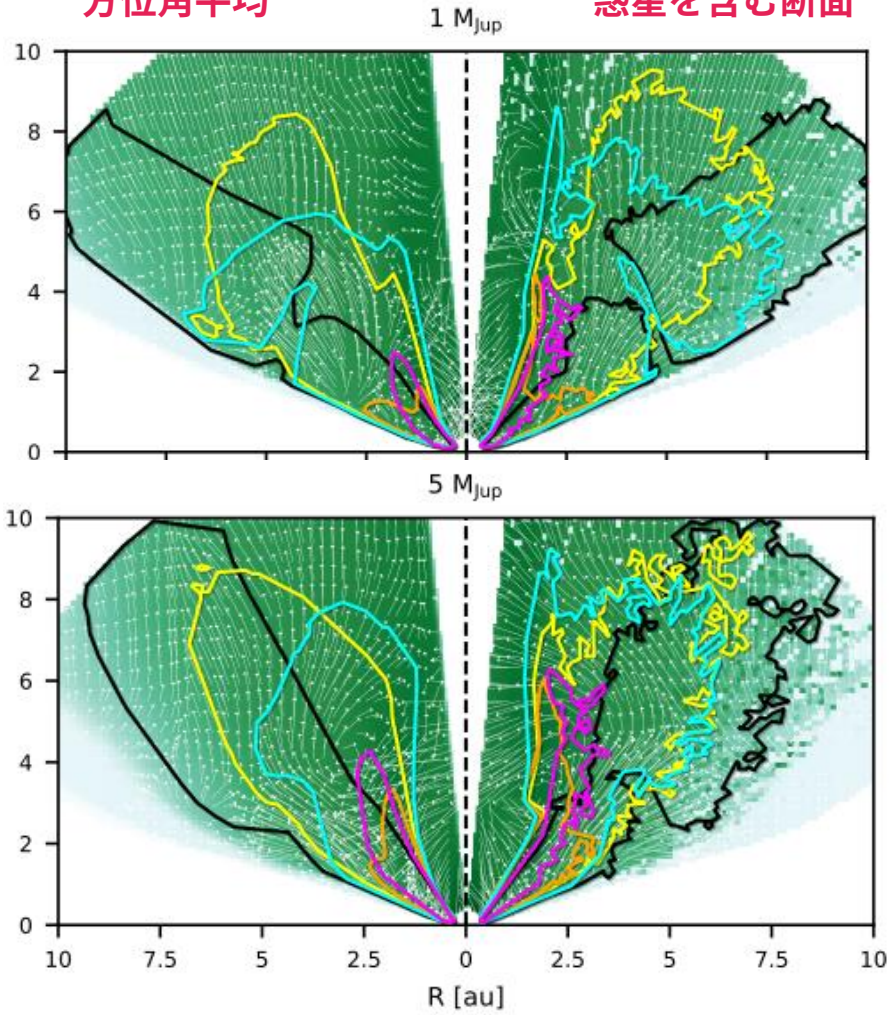

惑星を持つモデルでは、半径方向外側で放射量域が円盤表面よりも高い位置に押し上げられる。

[FeII]はこの影響が最も小さい。円盤風の立ち上がりのトレーサーとして利用できる。

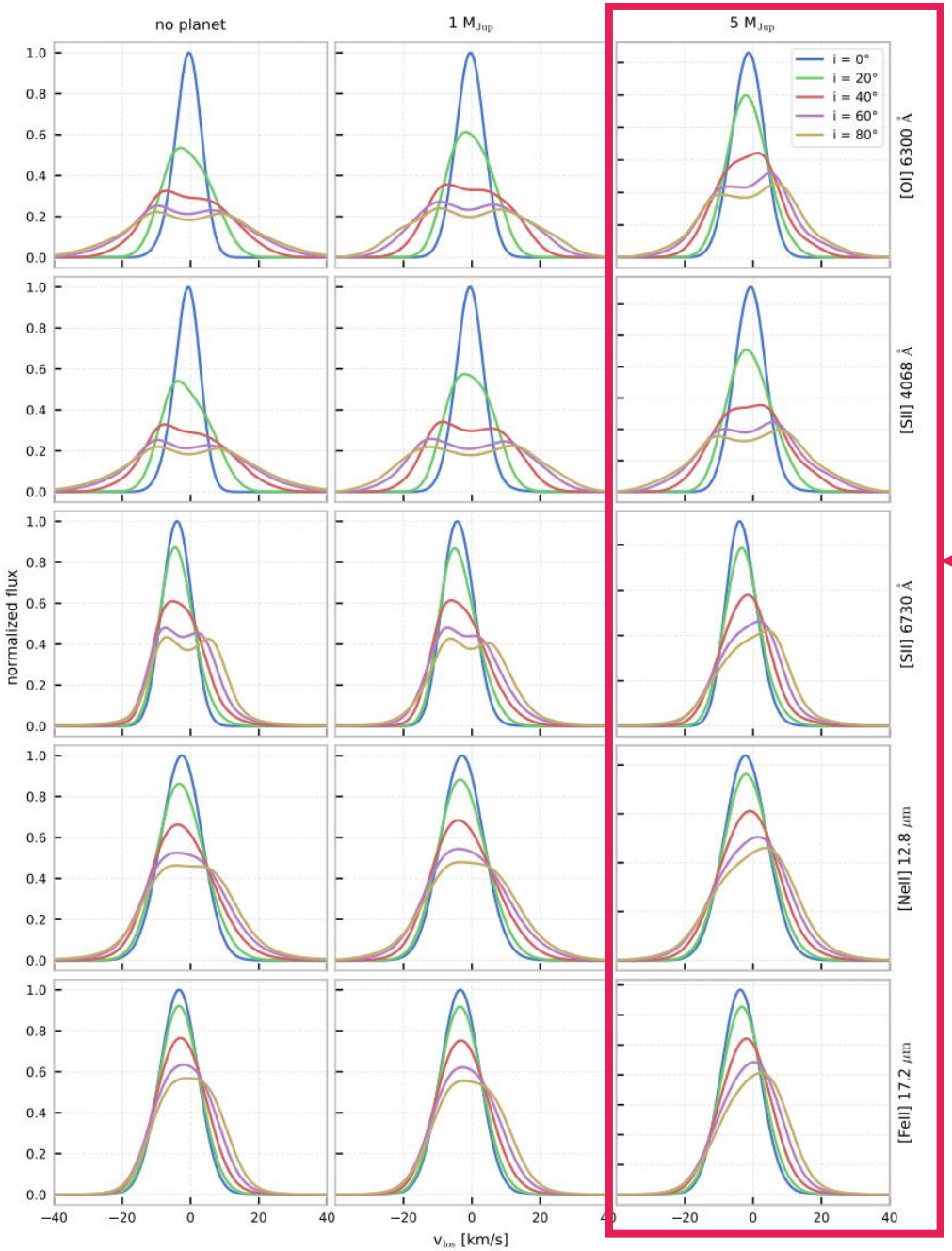

輝線プロファイル

有限のスペクトル分解能(可視光でR=100000, 中間赤外でR=60000)のもとでシミュレート

Model MJ1では惑星の影響は僅か。

Model MJ5では円盤風の構造変化が大きくなり、傾斜角が小さいと青方偏移が小さく、傾斜角が大きいと赤方偏移したピーク(観測者から遠ざかる方向の円盤風)が現れる。これは円盤の反対側にある遠ざかる円盤風からの寄与では説明できない。

現在得られている観測データと同程度のスペクトル分解能では違いは明確にならない

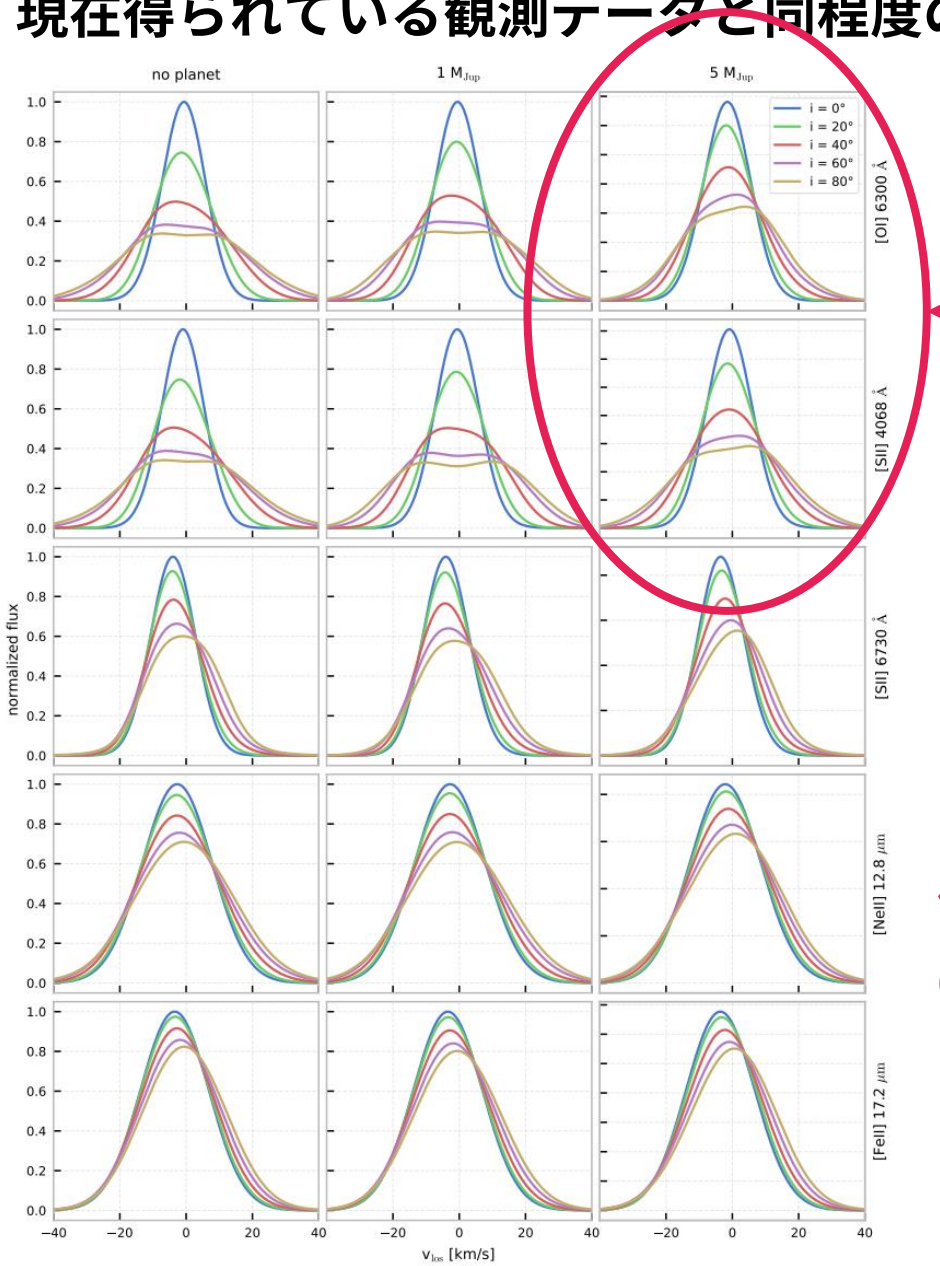

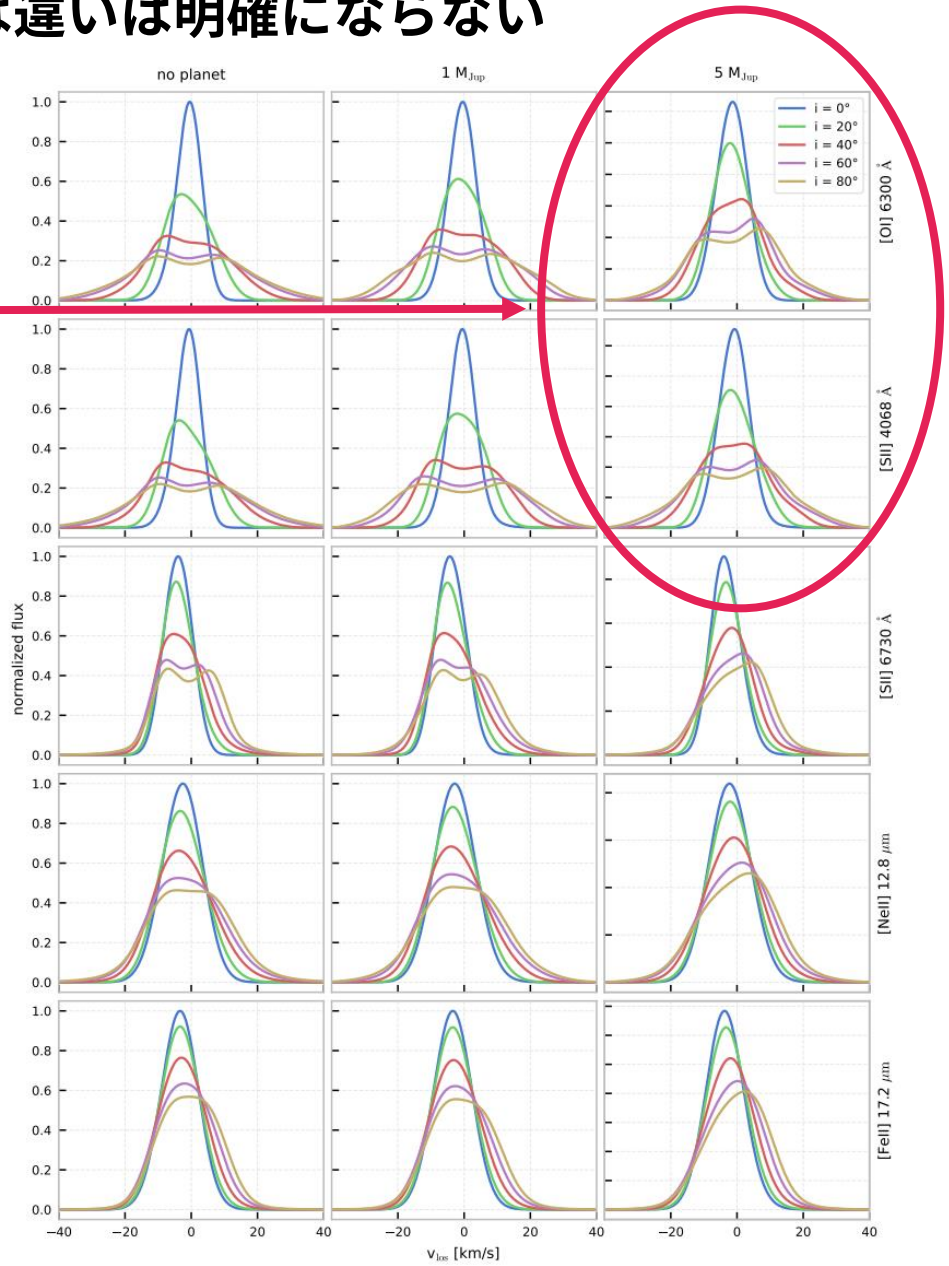

倍のスペクトル分解能
(将来観測)に期待

43. **Chemistry and dynamics of the prestellar core L1544**

O. Sipilä, P. Caselli, E. Redaelli, S. Spezzano ★ We aim to quantify the effect of chemistry on the infall velocity in the prestellar core L1544. Previous observational studies have found evidence for double-peaked line profiles for the rotational transitions of several molecules, which cannot be accounted for with the models presently available for the physical structure of the source, without ad hoc up-scaling of the infall velocity. We ran one-dimensional hydrodynamical simulations of the collapse of a core with L1544-like properties (in terms of mass and outer radius), using a state-of-the-art chemical model with a very large chemical network combined with an extensive description of molecular line cooling, determined via radiative transfer simulations, with the aim of determining whether these expansions of the simulation setup (as compared to previous models) can lead to a higher infall velocity. After running a series of simulations where the simulation was sequentially simplified, we found that the infall velocity is almost independent of the size of the chemical network or the approach to line cooling. We conclude that chemical evolution does not have a large impact on the infall velocity, and that the higher infall velocities that are implied by observations may be the result of the core being more dynamically evolved than what is now thought, or alternatively the average density in the simulated core is too low. However, chemistry does have a large influence on the lifetime of the core, which varies by about a factor of two across the simulations and grows longer when the chemical network is simplified. Therefore, although the model is subject to several sources of uncertainties, the present results clearly indicate that the use of a small chemical network leads to an incorrect estimate of the core lifetime, which is naturally a critical parameter for the development of chemical complexity in the precollapse phase.

- 星形成コアL1544の落下速度に対する化学的影響を定量可するため、コア崩壊の1次元流体シミュレーションを行った。
- 落下速度は化学ネットワーク・輝線冷却にほとんど依存しないことがわかった。
- 観測より示唆されている大きな落下速度の原因は化学進化ではない。(1)現在考えられているよりもコアの進化が進んでいるか、(2)計算したコアの平均密度が低すぎたことが原因と考えられる。
- 一方、化学的性質はコアの寿命に大きな影響を及ぼす(2倍ほど変化)。簡略化した化学進化計算を行うとコアの寿命の見積もりを誤らせることに注意が必要。

44. **Dust grains cannot grow to millimeter sizes in protostellar envelopes**

Kedron Silsbee, Vitaly Akimkin, Alexei V. Ivlev, Leonardo Testi, Munan Gong, Paola Caselli ★

A big question in the field of star and planet formation is the time at which substantial dust grain growth occurs. The observed properties of dust emission across different wavelength ranges have been used as an indication that millimeter-sized grains are already present in the envelopes of young protostars. However, this interpretation is in tension with results from coagulation simulations, which are not able to produce such large grains in these conditions. In this work, we show analytically that the production of millimeter-sized grains in protostellar envelopes is impossible under the standard assumptions about the coagulation process. We discuss several possibilities that may serve to explain the observed dust emission in the absence of in-situ grain growth to millimeter sizes.

- これまで、さまざまな波長帯で観測されたダスト放射は、若い原始星エンベロープにおけるミリメートルサイズのダスト粒子がすでに存在を示す証拠とされてきた。
- この解釈は、同じ条件下で大きなダスト粒子を作れない凝結シミュレーションの結果と矛盾する。
- 本研究では、凝固過程の標準的な想定のもとでは、原始星エンベロープでミリメートルサイズの粒子が作ることができないことを解析的に示す。
- ミリメートルサイズのダスト粒子がその場で成長しない場合に、観測されたダスト放射を説明するいくつかの可能性についても議論する。

45. **Stellar Flyby Analysis for Spiral Arm Hosts with Gaia DR3**

Linling Shuai, Bin B. Ren, Ruobing Dong, Xingyu Zhou, Laurent Pueyo, Robert J. De Rosa, Taotao Fang, Dimitri Mawet

★ Scattered light imaging studies have detected nearly two dozen spiral arm systems in circumstellar disks, yet the formation mechanisms for most of them are still under debate. Although existing studies can use motion measurements to distinguish leading mechanisms such as planet-disk interaction and disk self-gravity, close-in stellar flybys can induce short-lived spirals and even excite arm-driving planets into highly eccentric orbits. With unprecedented stellar location and proper motion measurements from Gaia DR3, here we study for known spiral arm systems their flyby history with their stellar neighbours by formulating an analytical on-sky flyby framework. For stellar neighbors currently located within 10 pc from the spiral hosts, we restrict the flyby time to be within the past 10^4 yr and the flyby distance to be within 10 times the disk extent in scattered light. Among a total of 12570 neighbors that are identified in Gaia DR3 for 20 spiral systems, we do not identify credible flyby candidates for isolated systems. Our analysis suggests that close-in recent flyby is not the dominant formation mechanism for isolated spiral systems in scattered light.

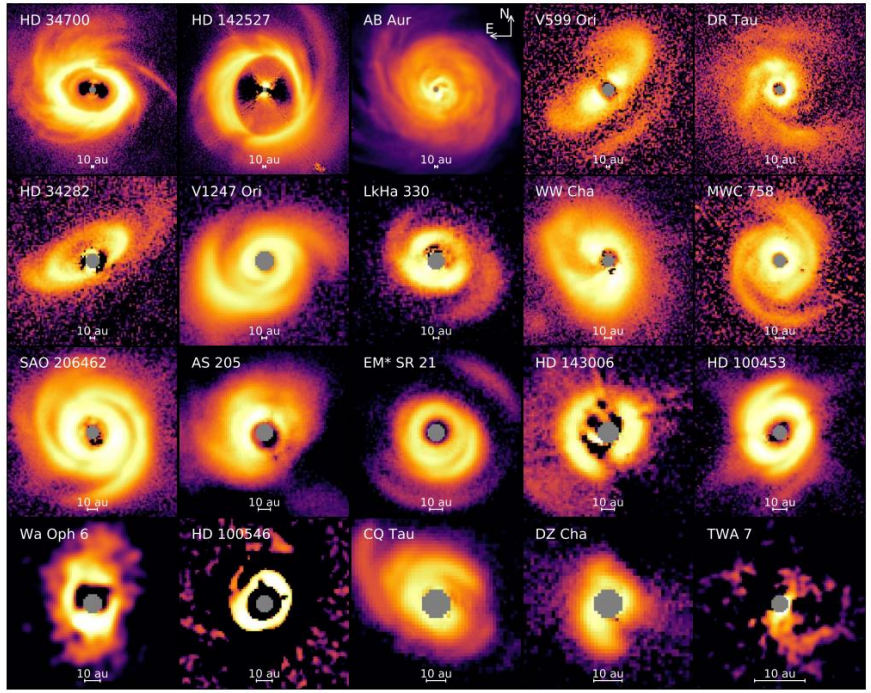

Figure 1. Gallery of spiral systems studied here for flyby analysis (color bar in log scale). The targets are sorted by decreasing physical extent from left to right, and top to bottom.

- 20の渦状腕系に対してGaia DR3で同定された合計12,570の近傍天体からは、孤立系への確かなフライバイ候補を同定することはできなかった。
- 近接フライバイは孤立した過剰腕系の主要な形成メカニズムではないことが示唆された。

46. Using debris disk observations to infer substellar companions orbiting within or outside a parent planetesimal belt

T. A. Stuber, T. Löhne, S. Wolf ★ Aims. We analyze whether the effects of secular perturbations, originating from a substellar companion, on the dust dynamics in a debris disk can be investigated with spatially resolved observations. Methods. We numerically simulated the collisional evolution of narrow and eccentric cold planetesimal belts around a star of spectral type A3V that are secularly perturbed by a companion that orbits either closer to or farther from the star than the belt. Based on the resulting spatial dust distributions, we simulated spatially resolved maps of their surface brightness in the K, N, and Q bands and at wavelengths of 70μm and 1300μm. Results. Assuming a nearby debris disk seen face-on, we find that the brightness distribution varies significantly with observing wavelength, for example between the N and Q band. This can be explained by the varying relative contribution of the emission of the smallest grains near the blowout limit. The orbits of both the small grains that form the halo and the large grains close to the parent belt precess due to the secular perturbations induced by a companion orbiting inward of the belt. The halo, being composed of older grains, trails the belt. The magnitude of the trailing decreases with increasing perturber mass and hence with increasing strength of the perturbation, a trend we recovered in synthetic maps of surface brightness by fitting ellipses to lines of constant brightness. Systems with an outer perturber do not show a uniform halo precession since the orbits of small grains are strongly altered. We identified features of the brightness distributions suitable for distinguishing between systems with a potentially detectable inner or outer perturber, especially with a combined observation with JWST/MIRI in the Q band tracing small grain emission and with ALMA at mm wavelengths tracing the position of the parent planetesimal belt.

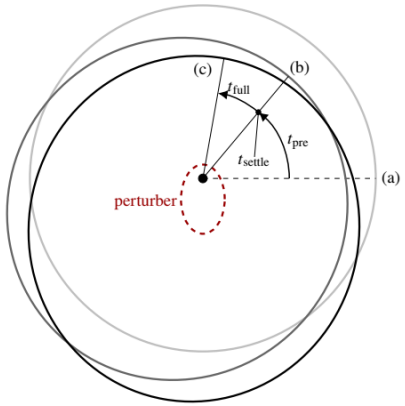

Fig. 1. Schematic representation of the belt orbits (solid gray and black) and the planet orbit (red) at the different stages of the ACE simulations: (*a*) the initial, circular, unperturbed belt; (*a, b*) the belt perturbed by the planet, but not modified by collisions; (*b*) the belt modified by collisions, but not by the perturber; (*b, c*) the belt modified by both the perturber and collisions.

- 伴星の重力ポテンシャルによる摂動がデブリ円盤に与える影響を数値シミュレーションし、空間分解観測によって確認可能かを調べる。

47. **Nonlinear Outcome of Coagulation Instability in Protoplanetary Disks II: Dust Ring Formation Mediated by Backreaction and Fragmentation**

Ryosuke T. Tominaga, Hidekazu Tanaka, Hiroshi Kobayashi, Shu-ichiro Inutsuka ★ In our previous work (Paper I), we demonstrated that coagulation instability results in dust concentration against depletion due to the radial drift and accelerates dust growth locally. In this work (Paper II), we perform numerical simulations of coagulation instability taking into account effects of backreaction to gas and collisional fragmentation of dust grains. We find that the slowdown of the dust drift due to backreaction regulates dust concentration in the nonlinear growth phase of coagulation instability. The dust-to-gas surface density ratio increases from 10^{-3} up to $\sim 10^{-2}$. Each resulting dust ring tends to have mass of $\simeq 0.5M_{\oplus} - 1.5M_{\oplus}$ in our disk model. In contrast to Paper I, the dust surface density profile shows a local plateau structure at each dust ring. In spite of the regulation at the nonlinear growth, the efficient dust concentration reduces their collision velocity. As a result, dust grains can grow beyond the fragmentation barrier, and the dimensionless stopping time reaches unity as in Paper I. The necessary condition for the efficient dust growth is (1) weak turbulence of $\alpha < 1 \times 10^{-3}$ and (2) a large critical velocity for dust fragmentation (> 1 m/s). The efficient dust concentration in outer regions will reduce the inward pebble flux and is expected to decelerate the planet formation via the pebble accretion. We also find that the resulting rings can be unstable to secular gravitational instability (GI). The subsequent secular GI promotes planetesimal formation. We thus expect that a combination of these instabilities is a promising mechanism for dust-ring and planetesimal formation.

- Paper II ...ガスへの逆反応・ダスト粒子の衝突破砕の影響を考慮した凝集不安定性の数値シミュレーションを行った。
- 効率的なダスト成長の必要条件：(1)α<1e-3の弱い乱流、(2)ダスト断片化の大きな臨界速度(>1[m/s])
- 外側領域でダストが効率よく濃縮されると、内側に向かうペブルフラックスが減少し、ペブル降着による惑星形成が減速する。その結果作られたリングは永年重力不安定性(GI)に対して不安定になり、惑星形成を促進する。

49. **Mid-Infrared Polarization of the Diffuse Interstellar Medium toward CygOB2-12**

Charles M. Telesco, Frank Varosi, Christopher Wright, Bruce T. Draine, Sergio Jose Fernández Acosta, Christopher Packham ★ We present the first mid-IR detection of the linear polarization toward the star CygOB2-12, a luminous blue hypergiant that, with AV of 10 mag of foreground extinction, is a benchmark in the study of the properties of dust in the diffuse interstellar medium. The 8-13 micrometer spectropolarimetry, obtained with the CanariCam multi-mode camera at the Gran Telescopio Canarias (GTC), shows clear trends with wavelength characteristic of silicate grains aligned in the interstellar magnetic field. The maximum polarization, detected with 7.8 statistical significance near 10.2 micrometers, is (1.24 +/- 0.28)% with position angle (126 +/- 8) deg. We comment on these measurements in the context of recent models for the dust composition in the diffuse interstellar medium.

- CygOB2-12 ... 前景に10光年程度の減光があるため、星間物質中の塵の性質を研究する上でベンチマークとなる青色超巨星
- この星に対する直線偏光を、中間赤外線で初めて検出された
- 8-13μmの分光偏光度は、星間磁場中で配列したケイ酸塩粒子に特有の波長を示す

50. **Ionisation of inner T Tauri star discs: effects of in-situ energetic particles produced by strong magnetic reconnection events**

Brunn V, Marcowith A, Sauty C, Padovani M, Rab C, Meskini C ★ Magnetic reconnection is one of the major particle acceleration processes in space and astrophysical plasmas. Low-energy supra-thermal particles emitted by magnetic reconnection are a source of ionisation for circumstellar discs, influencing their chemical, thermal and dynamical evolution. The aim of this work is to propose a first investigation to evaluate how energetic particles can propagate in the circumstellar disc of a T Tauri star and how they affect the ionisation rate of the disc plasma. To that end, we have collected experimental and theoretical cross sections for the production of H^+, H_2^+ and He^+ by electrons and protons. Starting from theoretical injection spectra of protons and electrons emitted during magnetic reconnection events, we have calculated the propagated spectra in the circumstellar disc considering the relevant energy loss processes. We have considered fluxes of energetic particles with different spectral indices and different disc magnetic configurations, generated at different positions from the star considering the physical properties of the flares as deduced from the observations obtained by the Chandra Orion Ultra Deep point source catalogue. We have then computed the ionisation rates for a disc whose structure has been calculated with the radiation thermo-chemical code `ProDiMo`. We find that energetic particles are potentially a very strong source of local ionisation with ionisation rates exceeding by several orders of magnitude the contribution due to X-rays, stellar energetic particles and radioactivity in the inner disc.

- 磁気リコネクションによって放出される低エネルギー粒子は、星周円盤の電離源となりその化学的・熱的・力学的進化に影響を与えることがわかっている。
- 本研究は、磁気リコネクションによって放出される高エネルギー粒子がどのように伝播して星周円盤プラズマの電離率に影響を与えるかを初めて調べた。
- 電子と陽子によるH+, H+2, He+の生成に関する実験と理論の断面積を集め、輻射熱化学コードProDiMoを用いて星周円盤の電離率を計算した。
- その結果、高エネルギー粒子は局所的な電離の非常に強い発生源であり、電離率は円盤の内側におけるX線・恒星高エネルギー粒子・放射線による寄与を数桁も上回ることがわかった。

51. **Residual Neural Networks for the Prediction of Planetary Collision Outcomes**

Philip M. Winter, Christoph Burger, Sebastian Lehner, Johannes Kofler, Thomas I. Maindl, Christoph M. Schäfer ★ Fast and accurate treatment of collisions in the context of modern N-body planet formation simulations remains a challenging task due to inherently complex collision processes. We aim to tackle this problem with machine learning (ML), in particular via residual neural networks. Our model is motivated by the underlying physical processes of the data-generating process and allows for flexible prediction of post-collision states. We demonstrate that our model outperforms commonly used collision handling methods such as perfect inelastic merging and feed-forward neural networks in both prediction accuracy and out-of-distribution generalization. Our model outperforms the current state of the art in 20/24 experiments. We provide a dataset that consists of 10164 Smooth Particle Hydrodynamics (SPH) simulations of pairwise planetary collisions. The dataset is specifically suited for ML research to improve computational aspects for collision treatment and for studying planetary collisions in general. We formulate the ML task as a multi-task regression problem, allowing simple, yet efficient training of ML models for collision treatment in an end-to-end manner. Our models can be easily integrated into existing N-body frameworks and can be used within our chosen parameter space of initial conditions, i.e. where similar-sized collisions during late-stage terrestrial planet formation typically occur.

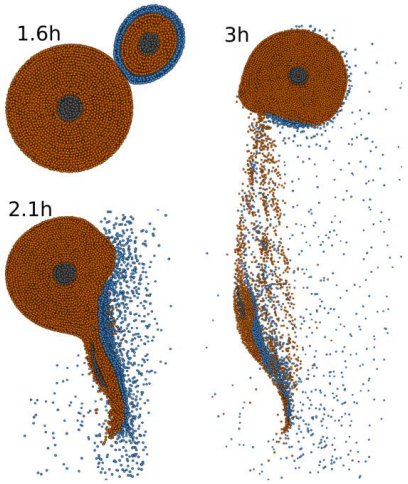

Figure 1. Exemplary snapshots at three different times of a SPH simulation of a planet-scale collision. The Mars-sized projectile hits the Earth-sized target at an impact angle of 43° and an impact velocity of 1.3 times the mutual escape velocity, resulting in a hit-and-run outcome. Colors indicate the different materials – an iron core, a silicate mantle, and a water/ice shell. Bodies are cut into halves for visualization. We perform 10164 collision simulations, covering a large parameter space of initial conditions.

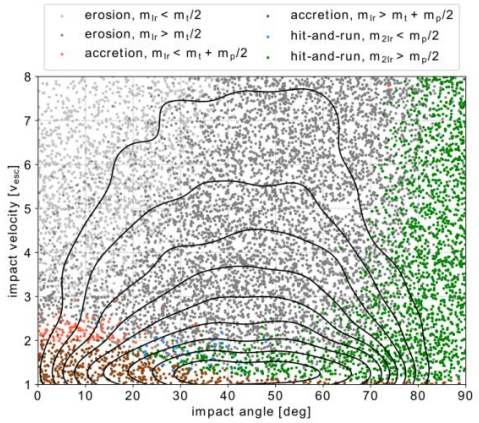

Figure 5. Overview of collision outcomes in impact angle – impact velocity space. Each datapoint represents a simulation in our SPH dataset. Colors indicate major outcome regimes: erosion (grayish), accretion (reddish), and hit-and-run (greenish). Each regime is further divided into sub-categories, depending on remnant masses. The contour overlay indicates collision statistics in a realistic dynamical environment, obtained from *N*-body simulations by Burger et al. (2020b), see Section 2.1.1. Contour levels correspond to iso-proportions of the density (in 10 per cent steps).

- 10164通りのSPH法による惑星間衝突シミュレーションのデータセットを作成した。これは惑星間衝突の研究における機械学習研究に利用できる。
- 今回は、衝突後の状態を予測する残差ニューラルネットワークによる機械学習モデルを構築した。

53. Discovery of non-metastable ammonia masers in Sagittarius B2

Y. T. Yan, C. Henkel, K. M. Menten, Y. Gong, H. Nguyen, J. Ott, A. Ginsburg, T. L. Wilson, A. Brunthaler, A. Belloche, J. S. Zhang, N. Budaiev, D. Jeff

★ We report the discovery of widespread maser emission in non-metastable inversion transitions of NH_3 toward various parts of the Sagittarius B2 molecular cloud/star forming region complex: We detect masers in the J, K = (6,3), (7,4), (8,5), (9,6), and (10,7) transitions toward Sgr B2(M) and Sgr B2(N), an NH_3 (6,3) maser in Sgr B2(NS), and NH_3 (7,4), (9,6), and (10,7) masers in Sgr B2(S). With the high angular resolution data of the Karl G. Jansky Very Large Array (JVLA) in A-configuration we identify 18 maser spots. Nine maser spots arise from Sgr B2(N), one from Sgr B2(NS), five from Sgr B2(M), and three in Sgr B2(S). Compared to our Effelsberg single dish data, the JVLA data indicate no missing flux. The detected maser spots are not resolved by our JVLA observations. Lower limits to the brightness temperature are >3000 K and reach up to several 10^5 K, manifesting the lines' maser nature. In view of the masers' velocity differences with respect to adjacent hot molecular cores and/or UCHII regions, it is argued that all the measured ammonia maser lines may be associated with shocks caused either by outflows or by the expansion of UCHII regions. Overall, Sgr B2 is unique in that it allows us to measure many NH_3 masers simultaneously, which may be essential to elucidate their so far poorly understood origin and excitation.

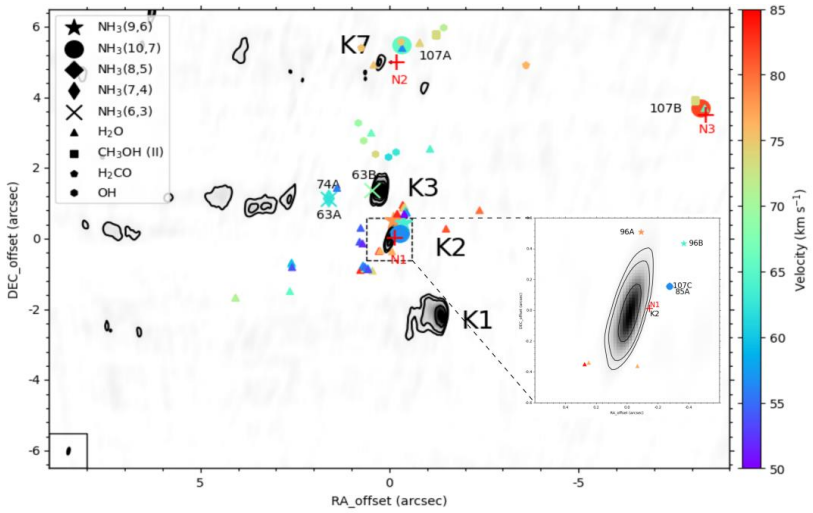

Fig. 2. JVLA 1.6 cm continuum map of Sgr B2(N), shown by the gray shaded areas and black contours with levels of 5, 10, 30, and 50 × 0.2 mJy beam^{-1}. The reference position is α_{J2000} = 17^{h}47^{m}19^s.883, and δ_{J2000} = −28°22′18″.412, the peak position of the continuum source K2. The crosses, thin diamonds, diamonds, stars, and circles show the positions of NH_3 (6,3), (7,4), (8,5), (9,6), and (10,7) emissions. H_2O (McGrath et al. 2004), class II CH_3OH (Caswell 1996; Lu et al. 2019), H_2CO (Mehringer et al. 1994; Hoffman et al. 2007; Lu et al. 2019), and OH (Gaume & Claussen 1990) masers are presented as triangles, squares, pentagons, and hexagons, respectively. The color bar indicates the velocity range (V_{LSR}) of maser spots. Red crosses mark the positions of the hot cores Sgr B2(N1), N2, and N3, taken from the 3 mm imaging line survey "Exploring Molecular Complexity with ALMA" (EMoCA, Bonfand et al. 2017). The systemic velocities of the hot cores N1, N2, and N3 are V_{LSR} = 64 km s^{-1}, V_{LSR} = 74 km s^{-1} and V_{LSR} = 74 km s^{-1}, respectively (Bonfand et al. 2017).

- Sgr B2においてNH3の広範囲なメーザー放射を発見した。
- 隣接する高温分子コアやUCHII領域との速度差を考慮すると、測定されたNH3メーザー線はすべて、アウトフローまたはUCHII領域の膨張による衝撃波に関連している可能性がある。

54. **Mass function of a young cluster in a low-metallicity environment. Sh 2-209**

Chikako Yasui, Naoto Kobayashi, Masao Saito, Natsuko Izumi, Yuji Ikeda ★ We present deep near-infrared (NIR) imaging of Sh 2-209 (S209), a low-metallicity ([O/H] = −0.5 dex) HII region in the Galaxy. From the NIR images, combined with astrometric data from Gaia EDR3, we estimate the distance to S209 to be 2.5 kpc. This is close enough to enable us to resolve cluster members clearly (≃1000 AU separation) down to a mass-detection limit of ≃0.1 $M_\odot$, and we have identified two star-forming clusters in S209, with individual cluster scales ∼1 pc. We employ a set of model luminosity functions to derive the underlying initial mass functions (IMFs) and ages for both clusters. The IMFs we obtained for both clusters exhibit slightly flat high-mass slopes ($\Gamma \simeq -1.0$) compared to the Salpeter IMF ($\Gamma = -1.35$), and their break mass of ≃0.1 $M_\odot$ is lower than those generally seen in the solar neighborhood (∼0.3 $M_\odot$). In particular, because the S209 main cluster is a star-forming cluster with a larger number of members (∼1500) than the number (∼100) in regions previously studied in such environments, it is possible for the first time to derive the IMF in a low-metallicity environment with high accuracy over the wide mass range 0.1–20 $M_\odot$.

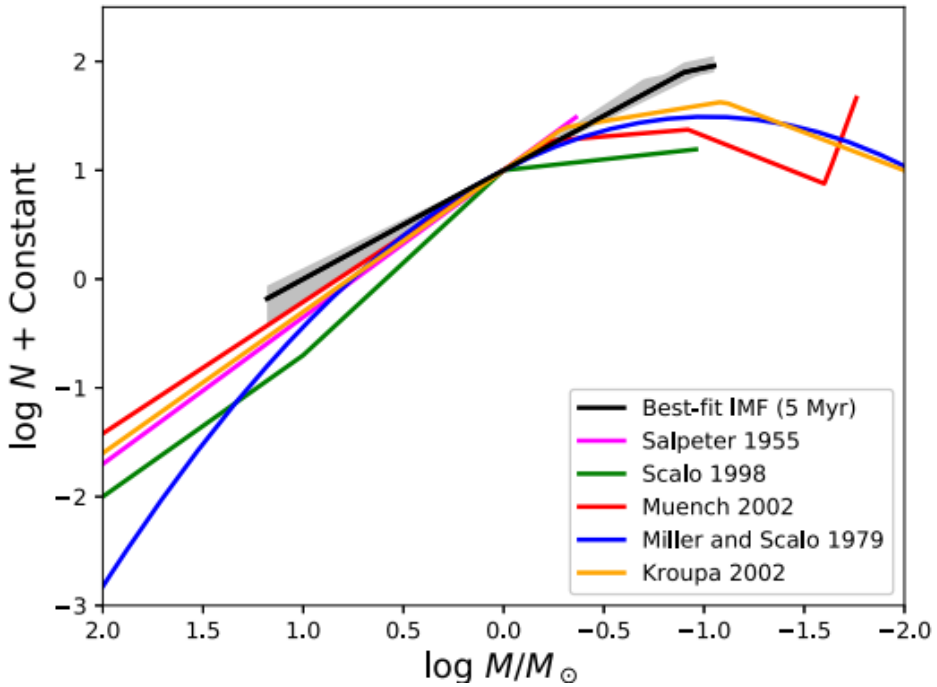

- 銀河系内の低金属度(O/H =-0.5 dex)HII領域・Sh 2-209(S209)の深い近赤外線(NIR)観測
- S209に2つの星形成星団を同定
- 特にS209主星団(約1500天体)は、従来の観測(約100天体)よりも多くの天体を持つため、低金属度環境におけるIMFを0.1-20Msunという広い質量範囲で導出することが初めて可能になった(左図best-fit IMF)。

55.

Dust extinction map of the Galactic plane based on the VVV survey data

Miaomiao Zhang, Jouni Kainulainen ★ Dust extinction is one of the most reliable tracers of the gas distribution in the Milky Way. The near-infrared (NIR) Vista Variables in the Via Lactea (VVV) survey enables extinction mapping based on stellar photometry over a large area in the Galactic plane. We devise a novel extinction mapping approach, XPNICER, by bringing together VVV photometric catalogs, stellar parameter data from StarHorse catalogs, and previously published Xpercentile and PNICER extinction mapping techniques. We apply the approach to the VVV survey area, resulting in an extinction map that covers the Galactic disk between 295 and 350 degrees at longitude and -2 to 2 degrees at latitude, and the Galactic bulge between -10 and 5 degrees at latitude. The map has 30 arcseconds spatial resolution and it traces extinctions typically up to about 10-20 mag of visual extinction and maximally up to Av 30 mag. We compare our map to previous dust based maps, concluding that it provides a high-fidelity extinction-based map, especially in its ability to recover both the diffuse dust component of the Galaxy and moderately extincted giant molecular cloud regions. The map is especially useful as independent, extinction-based data on the Galactic dust distribution and applicable for a wide range of studies from individual molecular clouds to the studies of the Galactic stellar populations.

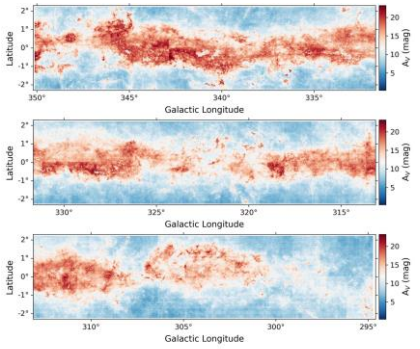

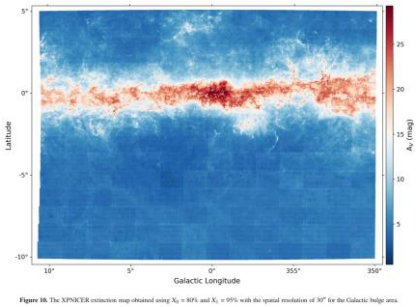

- ダスト減光 … 天の川におけるガス分布の最も信頼できるトレーサーの一つ
- XPNICERという新しい減光マッピング手法を考案し、銀河系円盤(295。<l<350°, -2。<b<2。)・銀河系バルジ(-10。<b<5。)をカバーする減光マップを作成した(左図)
- 従来の減光マップと比較すると、特に銀河の拡散ダスト成分と中程度に消滅した巨大分子雲領域の両方を再現する能力に優れる

56. **Turbulent Transport of Dust Particles in Protostellar Disks: The Effect of Upstream Diffusion**

Ting-Tao Zhou, Hongping Deng, Yi-Xian Chen, Douglas N. C. Lin ★ We study the long-term radial transport of micron to mm-size grain in protostellar disks (PSDs) based on diffusion and viscosity coefficients measured from 3D global stratified-disk simulations with a Lagrangian hydrodynamic method. While gas-drag tend to transport dust species radially inwards, stochastic diffusion can spread a considerable fraction of dust radially outwards (upstream) depending on the nature of turbulence. In gravitationally unstable disks, we measure a high radial diffusion coefficient Dr with little dependence on altitude. This leads to strong and vertically homogeneous upstream diffusion in early PSDs. In the solar nebula, the robust upstream diffusion of micron to mm size grains not only efficiently transports highly refractory mocron-size grains (such as those identified in the samples of comet 81P/Wild 2) from their regions of formation inside the snow line out to the Kuiper Belt, but can also spread mm-size CAI formed in the stellar proximity to distances where they can be assimilated into chondritic meteorites. In disks dominated by magnetorotational instability (MRI), the upstream diffusion effect is generally milder, with a separating feature due to diffusion being stronger in the surface layer than the midplane. This variation becomes much more pronounced if we additionally consider a quiescent midplane with lower turbulence and larger characteristic dust size due to non-ideal MHD effects. This segregation scenario helps to account for dichotomy of two dust populations' spatial distribution as observed in scattered light and ALMA images.

- 3次元層状円盤シミュレーションから得られた拡散係数と粘性係数を用いた、原始星系円盤（PSD）におけるミクロンからミリメートルサイズの微粒子の長期径方向輸送の研究
- ガス抵抗 ... 塵を半径方向内側(下流)に輸送する
- 確率的拡散 ... 乱流の性質によってかなりの割合の塵を半径方向外側(上流)に拡散させる
- 磁気回転不安定性が支配的な円盤では、拡散が中間面よりも表層で強くなることによってダスト集団が空間的に分離する特徴が見られる。